Stage long de recherche, FIP M1

Instabilité magneto-rotationnelle et disques d'accrétion: Étude numérique de la turbulence et effet des conditions aux limites

Magneto-rotational instability and accretion discs: Numerical study of the turbulence and influence of the boundary conditions

Emeric Bron

Stage réalisé avec Axel Brandenburg et Matthias Rheinhardt
à l'institut Nordita, Stockholm
du 1 Fevrier au 30 Juillet 2010

15 Août 2010

Résumé

My work during this internship consisted of numerical studies of the turbulence driven by the magneto-rotational instability in accretion discs. After a few preliminary works to familiarize myself with the code and with the physics, I studied the properties of this turbulence in the presence of a uniform gravity field, and then the influence of the boundary condition used, independently of any gravity field. In both cases, I studied the dependence on the magnetic Prandtl number and confirmed that there was no convergence problem in these situations. In a mean field perspective, I also tried to use the testfield method to measure the α and η tensors from mean field dynamo theory, and found that the Fourier space coefficients were necessary to reproduce the turbulent electromotive force. Other boundary conditions were also investigated without success.

Mon travail pendant ce stage a consisté en une étude via des simulations numériques de la turbulence déclenchée par l'instabilité magneto-rotationnelle dans les disques d'accrétion. Après quelques travaux préliminaires pour me familiariser avec le code et la physique du phénomène, j'ai étudié les propriétés de cette turbulence en présence d'un champ de gravité uniforme, puis l'influence du type de conditions aux limites que j'utilisais, indépendemment du champ de gravité. Dans les deux cas, j'ai étudié la dépendence en Pm, le nombre de Prandtl magnétique, et confirmé qu'il n'y avait pas de problème de convergence dans ces situations. Dans une optique de théorie de champ moyen, j'ai également utilisé la méthode des champs tests pour mesurer les tenseurs α et η de la "Mean Field Dynamo Theory", et ai trouvé que les coéfficients dans l'espace de Fourier étaient nécessaires pour reconstruire la force electromotrice turbulente. D'autres conditions aux limites ont également été essayées sans succès.

Contents

Introduction

Accretion discs are omnipresent astrophysical objects, from the protoplanetary disc to the infall of matter onto a supermassive black hole. Mainly composed of ionized gas, they are described within the framework of magnetohydrodynamics. In order to explain the observations, they are expected to be turbulent, a turbulence that must be triggered and driven by an instability. One main candidate has been found: the magneto-rotational instability (MRI).

Numerical simulations are a very useful tool to study complex magnetohydrodynamic flows like the turbulence driven by this instability, and can help to reach a better understanding of the mechanism of accretion discs.

During this internship, I worked on such numerical simulations of the MRI-driven turbulence in a local approximation of the flow in an accretion disc. I studied the properties of this turbulence and the influence of parameters, trying first to study the effect of a constant gravity field, and then more specifically the influence of a specific boundary condition. In a mean field theory perspective, I also aimed in both cases to build a mean field model of those situations by measuring coefficients relating the effects of the fluctuating fields to the mean fields.

My work consisted of many explorations, starting more paths than I could follow up during these six months.

The astrophysics group at Nordita

The Nordita institute in which I did my internship is a theoretical physics research institute, with groups working mainly on string theory and high energy physics, condensed matter physics, biological and statistical physics, and astrophysics.

The main component of the work of the astrophysics group, led by Axel Brandenburg, is on mean field dynamo theory, in particular applied to the sun and the generation of its magnetic field, but also to other astrophysical objects like galaxies or accretion discs. An important part of the work consists of numerical simulations done with the Pencil Code. Other subjects related to turbulence are also studied, like passive scalar transport, turbulent combustion, or influence of polymers.

Chapter 1

Theoretical basis

In this section, I will review a few fundamental concepts that were used in my work. After briefly recalling the magnetohydrodynamics (MHD) equations, I will describe the accretion disk model and the local approximation that are used in my simulations. I will then explain the basis of mean field dynamo theory. Although the situation that I studied contains no real dynamo, this mean field formalism will be used in the analysis in order to parameterize the effect of MHD turbulence from a mean field point of view.

1.1 Magneto Hydro Dynamics

Magnetohydrodynamics is the combination of hydrodynamics and electromagnetism in a conductive fluid. Astrophysical gases are in most of the cases at least partially ionized, allowing a coupling between the fluid motion and the magnetic field. This coupling leads to new behaviors of the fluid: waves (like the well known Alfven waves) and instabilities (like the magneto rotational instability, which I will describe later).

We will consider the plasma as a continuous medium, electrically neutral everywhere, and capable of conducting currents with a finite conductivity. The only microscopic effects that we will take into account are finite conductivity and a finite fluid viscosity. In such a case, the Ohm's law takes the form:

$$\boldsymbol{J} = \sigma(\boldsymbol{E} + \boldsymbol{U} \times \boldsymbol{B})$$

where σ is the conductivity of the fluid and $\boldsymbol{U}$ the fluid velocity.

In such a neutral medium, the Maxwell's equations can be written (we choose a unit system in which the vacuum permeability is unity, i.e. $\mu_0 = 1$):

$$\boldsymbol{\nabla} \cdot \boldsymbol{E} = 0 \tag{1.1}$$

$$\boldsymbol{\nabla} \times \boldsymbol{E} = -\frac{\partial \boldsymbol{B}}{\partial t} \tag{1.2}$$

$$\boldsymbol{\nabla} \cdot \boldsymbol{B} = 0 \tag{1.3}$$

$$\boldsymbol{\nabla} \times \boldsymbol{B} = \boldsymbol{J} + \frac{1}{c^2}\frac{\partial \boldsymbol{E}}{\partial t} \tag{1.4}$$

In this last equation, we will neglect the displacement current $\frac{1}{c^2}\frac{\partial \boldsymbol{E}}{\partial t}$. This term is negligible for phenomena in which propagation is slow compared to the speed of light and when the conductivity is sufficiently large. As we are interested in the coupling between the magnetic field and a non-relativistic fluid, we can neglect this term.

Combining the Ohm's law with equation (1.4) gives:

$$\boldsymbol{E} = \frac{1}{\sigma}\boldsymbol{\nabla} \times \boldsymbol{B} - \boldsymbol{U} \times \boldsymbol{B}$$

We define the magnetic diffusivity $\eta = \frac{1}{\sigma}$. Using this expression in equation (1.2) gives our evolution equation for the magnetic field, usually called the induction equation:

$$\frac{\partial \boldsymbol{B}}{\partial t} = \boldsymbol{\nabla} \times (\boldsymbol{U} \times \boldsymbol{B}) + \eta \Delta \boldsymbol{B} \tag{1.5}$$

The fluid motion obeys the usual momentum equation. As the fluid is supposed to be neutral, the Lorentz force is just $\boldsymbol{J} \times \boldsymbol{B}$. The equation of motion for the fluid is:

$$\rho \left[\frac{\partial \boldsymbol{U}}{\partial t} + (\boldsymbol{U} \cdot \boldsymbol{\nabla})\boldsymbol{U} \right] = -\boldsymbol{\nabla} P - \rho \boldsymbol{\nabla} \Phi + \boldsymbol{J} \times \boldsymbol{B} + \partial_j S_{ij} \tag{1.6}$$

where Φ is the gravitational potential and $S_{ij} = \rho\nu(\partial_j U_i + \partial_i U_j - \frac{2}{3}\delta_{ij}\partial_k U_k)$ is the viscous stress tensor.

We will consider only an isothermal fluid: $P = c_s^2 \rho$ with a constant c_s. This system of equation is then closed by the mass conservation equation:

$$\frac{\partial \rho}{\partial t} + \boldsymbol{\nabla} \cdot (\rho \boldsymbol{U}) = 0 \tag{1.7}$$

We will consider only constant ν and η.

1.2 Accretion disks, shearing box approximation and magneto-rotational instability

1.2.1 Accretion discs

When matter falls into a gravitational well, angular momentum conservation and interactions between fluid elements (pressure, viscosity, ...) give to this infall the shape of a disc. The accretion onto the central object takes place through the slowly spiraling orbit of the gas. Such accretion discs are present in any astrophysical situation where matter falls onto a massive object: a cloud collapsing onto a protostar, plasma from a star falling onto a compact companion in a binary system, matter falling in a supermassive black hole etc.

In order to go from one orbit to a lower one, the fluid element has to lose angular momentum. Angular momentum has to be transported outwards to allow an inwards

mass flux. The effective accretion rate is thus dependent on the angular momentum transport efficiency.

Moreover, the gas loses gravitational energy through accretion, and this energy is eventually converted into radiation. The radiative properties of the accretion disc, which are the only direct observables, are thus directly related to the accretion rate. Observations of accretion disks give then some clues on the angular momentum transport efficiency.

The simplest angular momentum transport mechanism is the effect of viscosity. A viscous fluid tries to resist against shearing, and thus transfers angular momentum outwards. But the microscopic viscosity of astrophysical gases is way to small to explain the observed luminosities. Another mechanism has to be found.

A more quantitatively detailed explanation of the angular momentum transport issue can be found in the review paper by Balbus & Hawley (1998) [1] . The complete calculation of the angular momentum flux shows that there is a non-viscous term due to correlations between components of the velocity field (Reynolds stress tensor) and between the component of the magnetic field (Maxwell stress tensor). For the radial angular momentum transport, the important component of the total stress tensor is:

$$W_{R\phi} = U_R U_\Phi - \frac{B_R B_\Phi}{\rho} \tag{1.8}$$

or some averaged value when global or intermediate scale properties are needed.

Such correlations can be present and important when turbulence occurs. Accretion discs are thus expected to be turbulent, in order to explain the observed accretion rates. Shakura and Sunyaev (1973)[2] proposed a phenomenological parametrization of turbulent disc models by scaling $W_{R\Phi}$ with c_s^2:

$$W_{R\Phi} = \alpha_{\rm SS} c_s^2 \tag{1.9}$$

where $\alpha_{\rm SS}$ is an adjustable parameter. The next step is to understand the physical mechanism of turbulence in accretion discs, and to see whether it gives reasonable values of $\alpha_{\rm SS}$.

We will here consider only a model with a very simple velocity field:

$$U_R = 0 \quad U_\Phi = \sqrt{\frac{GM}{R}} \quad U_z = 0 \tag{1.10}$$

where G is the gravitational constant, and M the mass of the central object. This field is an equilibrium solution of the equation of motion when viscosity is neglected. Each fluid element moves with the angular velocity corresponding to a keplerian orbit.

We will focus on the fluctuations around this large scale flow. In presence of a magnetic field, accretion discs are known to be unstable to the magneto-rotational instability (Balbus & Hawley 1991 [3]) that I will explain below. The simulations that I will present later aim to explore the properties of the magnetohydrodynamic turbulence triggered by this instability. In order to achieve sufficient resolution, these simulations will represent only a local region of the disc. I will use a classical approximation called the shearing box approximation.

1.2.2 The shearing box approximation

We will choose a point in the disk at a radius R_0 and follow the region around this point. It means that the frame of the simulation will rotate with the fluid at the angular velocity $\Omega_0 = \Omega(R_0)$ where $\Omega(R) = \sqrt{\frac{GM}{R^3}}$ is the keplerian angular velocity of the gas in the disk.

The large scale flow in this frame will then be:

$$U_R = 0 \quad U_\Phi = R\left(\sqrt{\frac{GM}{R^3}} - \sqrt{\frac{GM}{R_0^3}}\right) \quad U_z = 0$$

Keeping only the first order in $R - R_0 = r$ gives:

$$U_R = 0 \quad U_\Phi = -\frac{3}{2}\Omega_0 r \quad U_z = 0 \tag{1.11}$$

In this local approximation we will neglect all curvature terms. We can thus assimilate the cylindrical coordinates to a local cartesian coordinate system:

$$x = r \quad y = R\Phi \quad z = z$$

Depending on what we want to study, we can neglect or not the vertical stratification. In this section, I will do all calculations in the case when we neglect the vertical component of the gravity field (the local approximation is then around the mid-plane and neglect linear terms in z). Some of the simulations were done without this additional assumption. It adds one term in the momentum equation, and means that the initial stratification of the density is consistent with vertical hydrostatic equilibrium, instead of being uniform.

Let us write the set of equations that we will solve in this approximation. In order to trigger the magneto-rotational instability (see below), an external vertical uniform magnetic field B_0 will be present. Two cases are usually distinguished, depending on whether this initial magnetic field has a net vertical magnetic flux through the box or not. We are here in the finite net flux case, the other case is called zero net flux case (e.g. positive in one half of the box and negative in the other half).

We will solve for the fluctuating fields:

$$\boldsymbol{u} = \boldsymbol{U} + \frac{3}{2}\Omega_0 x \boldsymbol{e_y} \quad \text{and} \quad \boldsymbol{b} = \boldsymbol{B} - B_0 \boldsymbol{e_z}$$

We linearize the radial component of the gravity field:

$$-\boldsymbol{\nabla}\Phi = -\frac{GM}{R^2}\boldsymbol{e_R} \simeq -\frac{GM}{R_0^2}\left(1 - \frac{2x}{R_0}\right)\boldsymbol{e_x}$$

which is canceled by terms from the inertial forces:

$$-2\boldsymbol{\Omega_0} \times \boldsymbol{U} + (R_0 + x)\Omega_0^2 \boldsymbol{e_x} = -2\boldsymbol{\Omega_0} \times \boldsymbol{u} + \frac{GM}{R_0^2}\left(1 - \frac{2x}{R_0}\right)\boldsymbol{e_x}$$

The evolution equation are then:

$$\rho\left[\frac{\partial \boldsymbol{u}}{\partial t} + (\boldsymbol{u}\cdot\boldsymbol{\nabla})\boldsymbol{u} - \frac{3}{2}\Omega_0 x \partial_y \boldsymbol{u} - \frac{3}{2}\Omega_0 u_x \boldsymbol{e_y} + 2\boldsymbol{\Omega_0} \times \boldsymbol{u}\right] =$$
$$- c_s^2 \boldsymbol{\nabla}\rho + \boldsymbol{j} \times \boldsymbol{b} + \boldsymbol{j} \times \boldsymbol{B_0} + \partial_j s_{ij} - \nu\frac{3}{2}\Omega_0(\partial_y \rho \boldsymbol{e_x} + \partial_x \rho \boldsymbol{e_y}) \tag{1.12}$$

$$\frac{\partial \boldsymbol{b}}{\partial t} = \boldsymbol{\nabla} \times \left(\boldsymbol{u} \times \boldsymbol{b} + B_0 \boldsymbol{u} \times \boldsymbol{e_z} - \frac{3}{2}\Omega_0 x \boldsymbol{e_y} \times \boldsymbol{b} \right) + \eta \Delta \boldsymbol{b} \tag{1.13}$$

$$\frac{\partial \rho}{\partial t} + \boldsymbol{\nabla} \cdot (\rho \boldsymbol{u}) - \frac{3}{2}\Omega_0 x \partial_y \rho = 0 \tag{1.14}$$

where $s_{ij} = \rho\nu(\partial_j u_i + \partial_i u_j - \frac{2}{3}\delta_{ij}\partial_k u_k)$.

In order to find out the set of dimensionless parameters which parameterize this model, I will rewrite this equations in a non-dimensional form. I define the non-dimensional variables and coordinates:

$$\tilde{t} = \frac{t}{2\pi/\Omega_0} \quad \tilde{\boldsymbol{x}} = \frac{\boldsymbol{x}}{L} \quad \tilde{\rho} = \frac{\rho}{\rho_0} \quad \tilde{\boldsymbol{u}} = \frac{\boldsymbol{u}}{c_s} \quad \tilde{\boldsymbol{b}} = \frac{\boldsymbol{b}}{c_s\sqrt{\rho_0}}$$

where L is the size of the cubic domain.

We obtain then:

$$\begin{aligned}\tilde{\rho}\left[\frac{\partial \tilde{\boldsymbol{u}}}{\partial \tilde{t}} + \frac{1}{\mathrm{Ma}}(\tilde{\boldsymbol{u}}\cdot\tilde{\boldsymbol{\nabla}})\tilde{\boldsymbol{u}} - 3\pi\tilde{x}\partial_{\tilde{y}}\tilde{\boldsymbol{u}} - 3\pi\tilde{u_x}\boldsymbol{e_y} + 4\pi\boldsymbol{e_z}\times\tilde{\boldsymbol{u}}\right] = \\ -\frac{1}{\mathrm{Ma}}\tilde{\boldsymbol{\nabla}}\tilde{\rho} + \frac{1}{\mathrm{Ma}}(\tilde{\boldsymbol{j}}\times\tilde{\boldsymbol{b}} + \tilde{B_0}\tilde{\boldsymbol{j}}\times\boldsymbol{e_z}) \\ +\tilde{\partial}_j\left(\frac{1}{2\pi\mathrm{Re}}\tilde{\rho}[\tilde{\partial}_i\tilde{u_j} + \tilde{\partial}_j\tilde{u_i} - \frac{2}{3}\delta_{ij}\tilde{\partial}_k\tilde{u_k}]\right) - \frac{3}{2}\frac{\mathrm{Ma}}{\mathrm{Re}}(\partial_{\tilde{y}}\tilde{\rho}\boldsymbol{e_x} + \partial_{\tilde{x}}\tilde{\rho}\boldsymbol{e_y})\end{aligned} \tag{1.15}$$

$$\frac{\partial \tilde{\boldsymbol{b}}}{\partial \tilde{t}} = \frac{1}{\mathrm{Ma}}\tilde{\boldsymbol{\nabla}}\times(\tilde{\boldsymbol{u}}\times\tilde{\boldsymbol{b}} + \tilde{B_0}\tilde{\boldsymbol{u}}\times\boldsymbol{e_z}) - 3\pi\tilde{\boldsymbol{\nabla}}\times(\tilde{x}\boldsymbol{e_y}\times\tilde{\boldsymbol{b}}) + \frac{1}{2\pi\mathrm{Rm}}\tilde{\Delta}\tilde{\boldsymbol{b}} \tag{1.16}$$

$$\frac{\partial \tilde{\rho}}{\partial \tilde{t}} + \frac{1}{\mathrm{Ma}}\tilde{\boldsymbol{\nabla}}\cdot(\tilde{\rho}\tilde{\boldsymbol{u}}) - 3\pi\tilde{x}\partial_{\tilde{y}}\tilde{\rho} = 0 \tag{1.17}$$

where $\mathrm{Ma} = \frac{\Omega_0}{k_0 c_s}$ is the Mach number of the shear flow ($k_0 = 2\pi/L$), $\mathrm{Re} = \frac{\Omega_0}{\nu k_0^2}$ its Reynolds number, $\mathrm{Rm} = \frac{\Omega_0}{\eta k_0^2}$ its magnetic Reynolds number, and $\tilde{B_0} = \frac{B_0}{c_s\sqrt{\rho_0}}$ the dimensionless strength of the external magnetic field. These are the four parameters of our model. Instead of using Re and Rm, I will often use Rm and $\mathrm{Pm} = \frac{\mathrm{Rm}}{\mathrm{Re}}$, the magnetic Prandtl number.

The computational domain will be a cube, and we need boundary conditions that are consistent with the large scale shear flow. The simplest boundary conditions would be periodic boundary conditions but this would not enforce the shear flow. Along the x direction (radial direction), we will use what is called shearing periodic boundary conditions: as with periodic boundaries, each point on one boundary is identified with a point on the opposite boundary, but this identification is shifting with time at a velocity consistent with the shear flow. All variables are "periodic" in this sense (but our velocity variable does not represent the full velocity field, only the deviation from the shear flow).

For the other boundaries, we will use usual periodic boundary conditions along y (azimuthal direction). In the vertical direction, we will often use non-periodic boundaries, which will be discussed in the corresponding sections.

1.2.3 The Magneto Rotational Instability

As explained before, turbulence is expected to play a very important role in accretion discs by enhancing angular momentum transport. The search for an instability that would transform the laminar keplerian flow into a turbulent flow began in the purely hydrodynamic field. But keplerian flows are linearly stable, and no clue of a nonlinear instability was found, although non-rotating shearing flows with the same profile are unstable. Balbus and Hawley(1991)[3] showed that the presence of a weak magnetic field was sufficient to destabilize the flow, and the magneto-rotational instability (MRI) became the best candidate mechanism to trigger turbulence in accretion disk.

The basic idea of this instability is the following: The magnetic field tends to play the role of a spring between fluid elements. If two fluid elements initially very close are slightly displaced, one inwards and the other one outwards, the shear will cause the first one to be in advance compared to the second. The magnetic "spring" will then tend to slow down the first one and accelerate the second one. By doing that, it will transfer angular momentum from the first to second. Losing angular momentum, the inner element will fall in a lower orbit, while the outer one, gaining angular momentum, will go to a higher orbit. The radial separation will thus grow.

The shearing box model is of course also subject to this instability. I will detail here only the linear analysis of a simplified case in our local approximation. We will consider the ideal case, in which $\nu = \eta = 0$. Moreover, we will consider only the "axisymmetric" case (invariant along y), and even neglect variation along x in the final part in order to get a simple formula.

We will consider a small disturbance of our variables in Fourier space:

$$\tilde{\boldsymbol{u}} = \boldsymbol{\delta\tilde{u}}\ e^{i(\tilde{\omega}\tilde{t}-\tilde{\boldsymbol{k}}\cdot\tilde{\boldsymbol{x}})} \qquad \tilde{\boldsymbol{b}} = \boldsymbol{\delta\tilde{b}}\ e^{i(\tilde{\omega}\tilde{t}-\tilde{\boldsymbol{k}}\cdot\tilde{\boldsymbol{x}})} \qquad \tilde{\rho} = 1 + \delta\tilde{\rho}\ e^{i(\tilde{\omega}\tilde{t}-\tilde{\boldsymbol{k}}\cdot\tilde{\boldsymbol{x}})}$$

I will now forget the tildes on the dimensionless variables until the end of this section.

Using these expressions in our equations and keeping only the first order in the perturbation gives:

$$i\omega\delta u_x - 4\pi\delta u_y + ik_z\frac{B_0}{\mathrm{Ma}}\delta b_x - ik_x\frac{B_0}{\mathrm{Ma}}\delta b_z - ik_x\frac{1}{\mathrm{Ma}}\delta\rho = 0$$

$$\pi\delta u_x + i\omega\delta u_y + ik_z\frac{B_0}{\mathrm{Ma}}\delta b_y = 0$$

$$i\omega\delta u_z - ik_z\frac{1}{\mathrm{Ma}}\delta\rho = 0$$

$$ik_z\frac{B_0}{\mathrm{Ma}}\delta u_x + i\omega\delta b_x = 0$$

$$ik_z\frac{B_0}{\mathrm{Ma}}\delta u_y + 3\pi\delta b_x + i\omega\delta b_y = 0$$

$$ik_x\frac{B_0}{\mathrm{Ma}}\delta u_y + i\omega\delta b_z = 0$$

$$-ik_x\frac{1}{\mathrm{Ma}}\delta u_x - ik_z\frac{1}{\mathrm{Ma}}\delta u_z + i\omega\delta\rho = 0$$

The dispersion relation is then obtained by taking the determinant of the corresponding matrix equal to zero.

We will do it only in the case $k_x = 0$. In this case, the density loses its coupling with the rest of the problem, giving independently acoustic waves in the u_z variable, and b_z also disappears from the problem. This is not the case in the full three dimensional situation, but as the one dimensional modes are the fastest growing one, the growth rates that we will get here stay a good prediction for simulations in the first part of the exponential growth.

The dispersion relation is here:

$$\omega^4 - [(2\pi)^2 + 2\frac{B_0^2}{\mathrm{Ma}^2}(2\pi)^2 k_z^2]\omega^2 - 3(2\pi)^4\frac{B_0^2}{\mathrm{Ma}^2}k_z^2 + \frac{B_0^4}{\mathrm{Ma}^4}(2\pi)^4 k_z^4 = 0$$

We are looking for an instability, so we want the complex solutions for ω, with a negative imaginary part. The growth rate λ is then:

$$\lambda = i\omega = \sqrt{\frac{1}{2}\Big(- (2\pi)^2 - 2\frac{B_0^2}{\mathrm{Ma}^2}(2\pi)^2 k_z^2 + \sqrt{(2\pi)^4 + 16(2\pi)^4\frac{B_0^2}{\mathrm{Ma}^2}k_z^2}\Big)}$$

from which we can calculate the fastest growing wavenumber and its growth rate:

$$\tilde{k_z}_{max} = \frac{\sqrt{15}}{4}\frac{\mathrm{Ma}}{\tilde{B_0}} \qquad \tilde{\lambda}_{max} = \frac{3}{2}\pi$$

A simple way to understand the effect of non-zero diffusivities (ν and η), is to consider a simplified viscous diffusion operator $\rho\nu\boldsymbol{\Delta u}$. In this case, the ω terms are replaced by $\omega + i\frac{1}{2\pi\mathrm{Re}}k_z^2$ or $\omega + i\frac{1}{2\pi\mathrm{Rm}}k_z^2$. In the case $\mathrm{Pm} = 1$, it simply decreases the growth rate by $-\frac{1}{2\pi\mathrm{Rm}}k_z^2$. This implies that in the non-ideal case, the growth rate (of the fastest growing mode) becomes dependent on the field strength, and that the fastest growing wavenumber starts to be non-monotonic in the field strength.

1.2.4 The convergence problem

When investigating the properties of the MRI-driven turbulence with numerical simulations, a problem was found. Realistic astrophysical situations correspond to very low magnetic Prandtl numbers, and numerical simulations without stratification in a fully periodic box showed that the intensity of the turbulence and the angular momentum transport parameter α_{SS} were decreasing when Pm was decreasing, both in the zero net flux case (Fromang & Papaloizou 2007 [4]) and in the finite net flux case (Lesur & Longaretti 2007 [5]). This is what is called the convergence problem.

This problem is not present in stratified simulations (with a linear gravity field), and a recent paper by Käpylä & Korpi (2010) [6] showed that it also disappeared in zero net flux non-stratified simulations when using open boundaries like vertical field boundary conditions in the z direction for the magnetic field (tangential components are zero at the two boundaries).

1.3 Mean field theory and testfield method

1.3.1 Mean field theory

The idea of a mean field theory is to reduce the complexity of a turbulent flow to a more simple model where one is interested only in the evolution of the mean variables (different averaging procedures can be used). The difficulty is to understand the interactions between the mean field and the fluctuating field, and to introduce equivalent effects in the purely mean field evolution equation.

Here, we will be interested in the evolution of the mean magnetic field, and use the mean field formalism that has been developed for the study of dynamo problems (Moffatt 1978[7], Krause & Rädler 1980[8]). If we write the induction equation for the mean magnetic field (for any averaging procedure that respect the Reynolds rules), splitting the magnetic field into: $\boldsymbol{B} = \overline{\boldsymbol{B}} + \boldsymbol{b'}$ (and idem for the velocity field), we get:

$$\frac{\partial \overline{\boldsymbol{B}}}{\partial t} = \boldsymbol{\nabla} \times (\overline{\boldsymbol{U}} \times \overline{\boldsymbol{B}} + \overline{\boldsymbol{u'} \times \boldsymbol{b'}}) + \eta \Delta \overline{\boldsymbol{B}} \tag{1.18}$$

We see that the effect of the fluctuating field manifests itself in the term $\overline{\boldsymbol{u'} \times \boldsymbol{b'}}$. In order to get a mean field model, it is necessary to find a way to express this effect as a function of the mean fields only.

From the evolution equation of the fluctuating field:

$$\frac{\partial \boldsymbol{b'}}{\partial t} = \boldsymbol{\nabla} \times (\overline{\boldsymbol{U}} \times \boldsymbol{b'} + \boldsymbol{u'} \times \overline{\boldsymbol{B}} + \boldsymbol{u'} \times \boldsymbol{b'} - \overline{\boldsymbol{u'} \times \boldsymbol{b'}}) + \eta \Delta \boldsymbol{b'} \tag{1.19}$$

We see that $\boldsymbol{b'}(\boldsymbol{u'}, \overline{\boldsymbol{U}}, \overline{\boldsymbol{B}})$ is linear and homogeneous in $\overline{\boldsymbol{B}}$, and the same is then true for $\overline{\boldsymbol{u'} \times \boldsymbol{b'}}$.

The usual ansatz for $\overline{\boldsymbol{u'} \times \boldsymbol{b'}}$, neglecting time variability and higher spatial derivatives than the first, is:

$$(\overline{\boldsymbol{u'} \times \boldsymbol{b'}})_i = \alpha_{ij} \overline{B}_j - \eta_{ijk} \partial_j \overline{B}_k \tag{1.20}$$

In my work, I will only use averages on xy-planes: $\overline{X}(z,t) = \frac{1}{L^2} \int \int X(x,y,z,t) dxdy$ because the only expected and interesting inhomogeneity will be along the z direction (stratification or non-periodic boundary conditions).

In this case, we can simplify the ansatz by redefining η:

$$(\overline{\boldsymbol{u'} \times \boldsymbol{b'}})_i(z,t) = \alpha_{ij}(z,t) \overline{B}_j(z,t) - \eta_{ij}(z,t) \overline{J}_j(z,t) \tag{1.21}$$

with i and j being 1 or 2.

This relation takes non-locality effects into account only by the first derivative. A more precise way is to represent the non-local spatial dependences in Fourier space:

$$(\overline{\boldsymbol{u'} \times \boldsymbol{b'}})_i(z,t) = \int dk (\hat{\alpha}_{ij}(k,z,t) \hat{\overline{B}}_j(k,t) - \hat{\eta}_{ij}(k,z,t) \hat{\overline{J}}_j(k,t)) e^{ikz} \tag{1.22}$$

The integration will become a discrete sum in finite size boxes.

1.3.2 The testfield method

The next step is to find an expression for the α and η tensors in the mean field model. To achieve this goal, it is necessary in a first time to try to measure these tensors in a full non mean field simulation.

A method to do this has been developed: the testfield method (Schrinner et al. 2005, 2007 [9, 10], Rheinhardt & Brandenburg 2010 [11]).

Due to the linearity of equation (1.19) and of the fluctuating EMF $\overline{\boldsymbol{u'} \times \boldsymbol{b'}}$, we can solve this equation for arbitrary testfields $\overline{\boldsymbol{B}}^T$ and get a $\overline{\boldsymbol{u'} \times \boldsymbol{b'}}^T$ which depends linearly on $\overline{\boldsymbol{B}}^T$. Applying relation 1.21 gives:

$$(\overline{\boldsymbol{u'} \times \boldsymbol{b'}})_i^T = \alpha_{ij} \overline{B}_j^T - \eta_{ij} \overline{J}_j^T$$

When doing this for a set of independent testfields, it will give a system of linear equations, from which we can calculate the α and η tensors. Due to linearity, this result will be independent of the testfields that are used.

For the simple ansatz, we can use the following set of testfields:

$$\overline{\boldsymbol{B}}^{(1)} = b_0 \boldsymbol{e_x} \quad \overline{\boldsymbol{B}}^{(2)} = b_0 \boldsymbol{e_y} \quad \overline{\boldsymbol{B}}^{(3)} = b_0 z \boldsymbol{e_x} \quad \overline{\boldsymbol{B}}^{(4)} = b_0 z \boldsymbol{e_y}$$

If we want the Fourier space k-dependent tensors, we will use sinusoidal testfields with the set of values of k that we want to take into account.

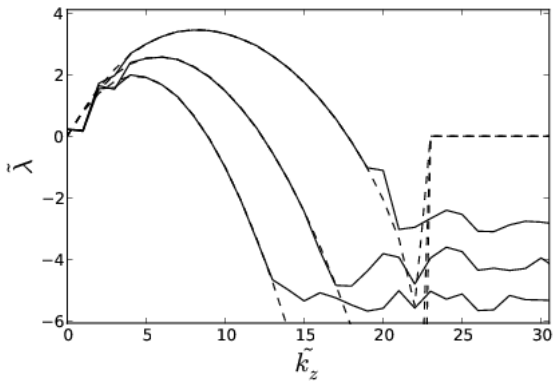

Figure 1.1: Growth rate as a function of the wave number for 1D runs with Rm=110, 200 and 500 (solid lines), compared with the theoretical predictions (dashed lines)

Chapter 2

Simulations

2.1 Preliminary work

I started by doing simple simulations in order familiarize myself with the code that I would use. The Pencil Code is a high order finite difference code for magnetohydrodynamics, but its modular conception allowed it to grow into a very polyvalent tool, used for various purposes, from turbulent chemistry to particles transport.

This code has already been used for local simulations of accretion discs and the corresponding setup was thus already prepared. In order to learn to use it, understand the various data produced, and get used to manipulate and visualize these data by writing small Python scripts, I started with very simple 1-dimensional situations, and then slowly increased the complexity. It was also an occasion to familiarize myself with the MRI and MHD turbulence. In all those simulations the boundary condition in the z direction was simply periodic.

2.1.1 1D simulations

The first goal was to check the analytical results of the linear stability analysis by measuring the growth rate of the instability and its dependence on parameters. In the 1D case, the instability does not break into turbulence and only the exponential growth is visible.

I measured the growth rate as a function of the wavenumber for various values of Rm in the $\mathrm{Pm} = 1$ case (which is easily calculable analytically). A few of these measurements are shown on Figure 1.1, with very good agreement between the numerical results and the analytical predictions. I also tried briefly varying the imposed field strength and the physical dimensions of the box, again with results consistent with the analytical calculations.

2.1.2 2D simulations

I then tried adding the radial (along x) variability. In this 2D case, the initial exponential growth reaches a saturation point after which a steady turbulent state appears (cf. left

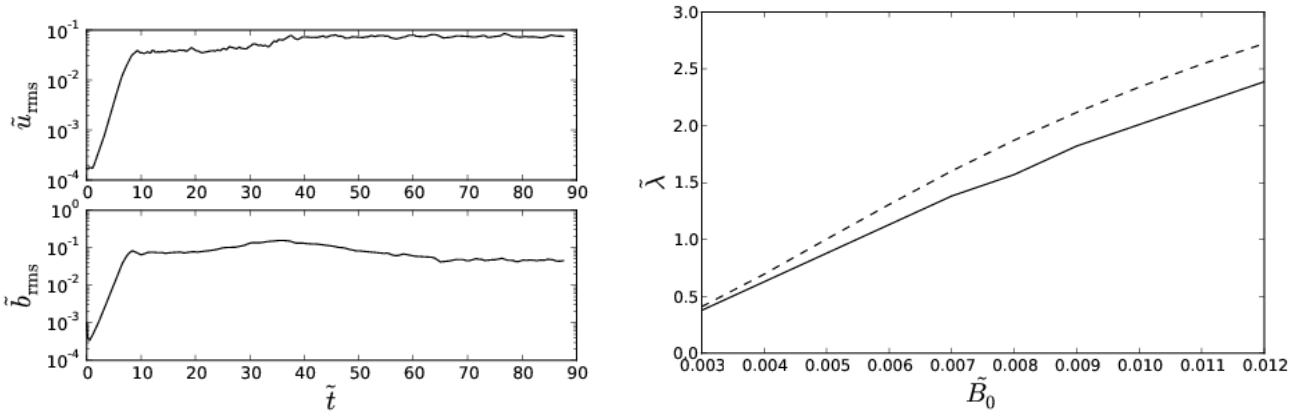

Figure 2.1: (Left): Typical time series of a 2D run. (Right): Growth rate as a function of the dimensionless imposed field amplitude for 2D runs with Rm=500 and Pm=1 (solid line), compared with the theoretical prediction (dashed line).

panel of Figure 2.1). The 1D modes happen to be the fastest growing modes, which makes the 1D analysis still a good approximation for the beginning of the exponential growth stage. Measuring the growth rate of the root mean square values of the variables (which converge toward the growth rate of the fastest growing mode) confirmed a rather good consistency with the 1D analysis (cf. right panel of Figure 2.1).

While starting to explore the parameter space, I could see that in some region the simulations were crashing. The Pencil Code uses an adaptive timestep following the Courant-Friedrichs-Lewy condition in order to stay stable, but in some case it is not sufficient and the timestep starts decreasing exponentially, effectively stopping the simulation. The next goal was then to determine the accessible regions of the parameter space, with respect to Re, Rm and $\tilde{B}_0$. Figure 2.2 shows some of the results (for Ma = 0.22, I also did some tries for Ma = 0.11, with consistent results).

2.1.3 3D fully periodic box simulations

I then started doing 3-dimensional simulations in a fully periodic box. This time, the goal was to study the behavior of the MRI when approaching the instability threshold by decreasing Rm, and to see if the level of the turbulence after saturation (measured by the root mean square values of the variables) would decrease toward zero when approaching the threshold or jump to zero from a non-zero value. These simulations were done for Pm = 1 and Ma = 0.1.

The results are shown on Figure 2.3 (left panel). The error bars are calculated by dividing the time series in three equal parts, calculating the average on each part, and taking the minimum and maximum values as bounds of the error range. The same procedure will be used for all error bars in this report.

The unexpected result is that while $u_{\rm rms}$ is decreasing, $b_{\rm rms}$ seems to increase when approaching the threshold. This is due to the appearance of a new phenomenon: after the

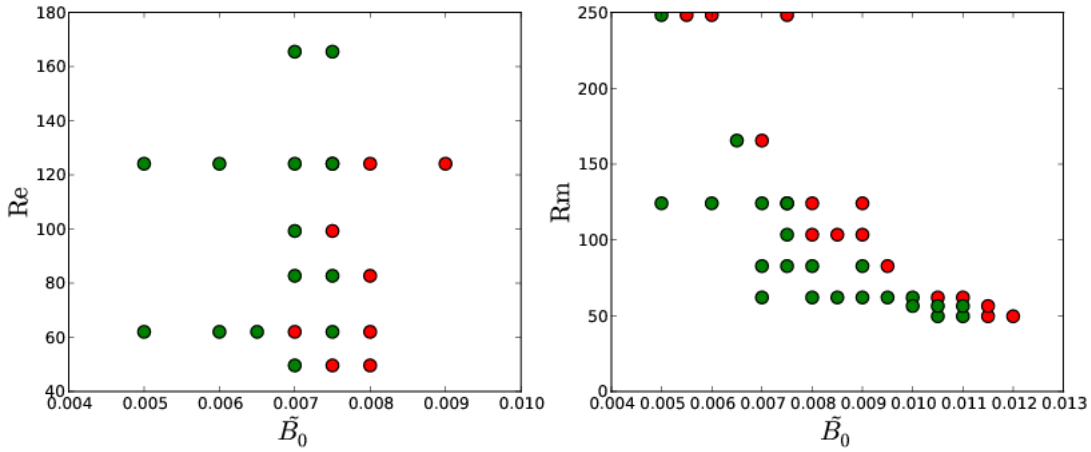

Figure 2.2: Outcome of the run depending on its parameters for fixed Rm = 125 (left) and for fixed Re = 125 (right), red dots mean crashing runs (due to insufficient number of mesh points), green dots non-crashing runs.

initial saturation, the turbulence becomes unsustainable for low Rm and starts to decay until the MRI can start again. We then see a succession of bursts as shown on the right panel of Figure 2.3, the growth rate during each burst being consistent with analytical predictions. Surprisingly, it seems that these bursts increase the time averaged value of $b_{\rm rms}$. This behavior when approaching a threshold of the MRI was already described in Lesur & Longaretti (2007).

Unfortunately, as I also started the study described in the next section, this subject was put aside and never finished. The computational time required when approaching the threshold was actually increasing, because the MRI growth rate is decreasing toward zero, making the burst duration longer, and thus the time required to do a correct average.

2.2 Stratified box simulations

2.2.1 Introduction

The goal of this set of simulations was to study the effect of a constant gravity field on the MRI-driven turbulence. Numerical studies of the MRI are usually either without any stratification, or with a linear gravity field, then representing the mid-plane where the gravity field is zero and the two hemispheres where it has opposite signs.

The situation that is studied here corresponds to an intermediate step: the vertical inhomogeneity is reduced to the minimum, the gravity field being not height-dependent itself, and no particular position like a mid-plane is present in the box. This setup represents a local approximation at some height z_0 in the disk.

The aim is to determine the effect of this gravity field on the properties of the MRI-

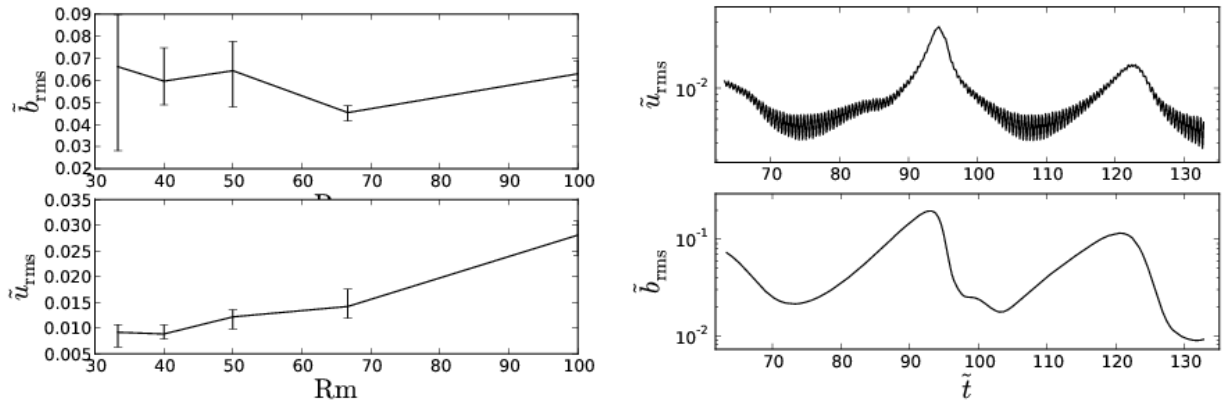

Figure 2.3: Time average of the rms values of the variables depending on Rm (left) and time series of the late stage of a run with Rm = 40 showing an episodic behavior(right).

driven turbulence, specifically its intensity measured by the root mean square values of the variables, and the angular momentum transport parameter $\alpha_{\rm SS}$, but also the transport coefficients α and η from the mean field dynamo theory, in order to be able to deduce a simplified mean field model for this situation.

Another goal is to determine what is the situation in this case with respect to the convergence problem, by studying the dependence on the magnetic Prandtl number Pm of the intensity of the turbulence.

In this case, due to the vertical variation of the gravitational potential energy, it is not possible to use periodic boundary conditions for the top and bottom boundaries. Instead, stress-free boundary conditions will be used for the fluid velocity field (no normal component and no shear stress at the boundary). For the magnetic field, we will use a normal field boundary condition, which is consistent with the presence of a vertical imposed field, and is one of the simplest open boundary (field lines can cross the boundary), which allows the variation of the volume averaged magnetic field.

To sum up the configuration, this set of runs include linear keplerian shear with shearing periodic boundaries along the x direction, rotation, an imposed vertical magnetic field and a constant gravity field. The values of the parameters will be in the following ranges: Ma = 0.1, Pm = 0.5 − 2, Rm = (0.5–1) × 10^2, $\tilde{B}_0 = 0.003$. The dimensionless strength of the gravity field is $\frac{2\pi}{c_s\Omega_0}g = 10\pi$ in all the simulations.

2.2.2 Time evolution and mean field profile

The simulation is evolved until a steady saturated state is reached. Figure 2.4 shows the time evolution of the root mean square values of the velocity and magnetic field. At first, we see an exponential growth corresponding to the linear stage of the magneto-rotational instability. Because of the variation of the density throughout the box, the growth rate is not the same in every part of the box, resulting in a non-constant (instantaneous) growth rate that we see at the beginning. When reaching the saturation of this linear

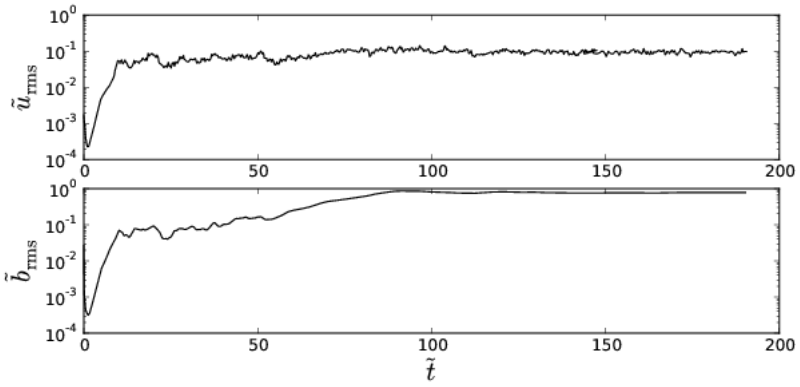

Figure 2.4: Time evolution of the root mean square values of the velocity and magnetic fields in a stratified simulation

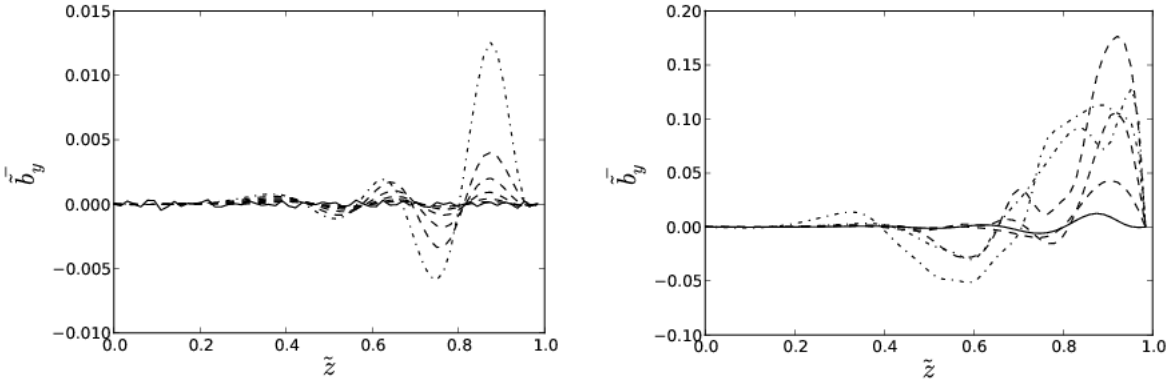

Figure 2.5: Successive profiles of the mean magnetic field $\overline{\tilde{b}_y}$ during the linear growth phase (left, from $\tilde{t} = 0$ to 6) and during the saturation (right, from $\tilde{t} = 6$ to 16).

phase, we see that we do not immediately reach a steady state, but go through a quite long transitory stage, during which B_{rms} increases by one order of magnitude (while U_{rms} does not vary much).

Looking at the evolution of the mean field profile (Figure 2.5), we see the height dependent growth rate (roughly compatible with the analytical solution calculated from the local value of density at this point) of pseudo-sinusoidal perturbations during the first linear phase, and then non-linear saturation occurring first in the less dense part of the box and then propagating downward.

After this saturation, it seems at first that a steady turbulent state has been reached, but looking at the evolution diagram of the mean magnetic field (Figure 2.6) shows that after a few tens of orbital periods, the mean field starts to grow, gaining one order of magnitude, and reaches the profile shown on Figure 2.7. A transition seems to occur

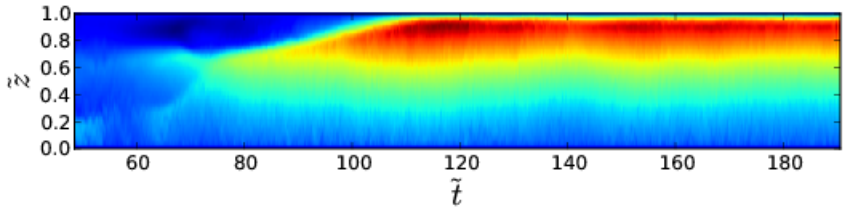

Figure 2.6: Time evolution of the y component of the mean magnetic field, showing the transition in the mean field geometry.

from a field concentrated in the less dense part of the box, to a field filling the whole box, with a marked stratification.

The y component is two orders of magnitude higher than the x component, which is often the case in shearing flows, due to the fact that the shear tends to transform field along x into field along y. A surprising detail is the strong gradients of $\tilde{b}_y$ near the boundaries, and the strong peaks of $\tilde{b}_x$ at the same places. Those strong gradients and peaks mean strong dissipation, showing that a strong turbulent electromotive force is present near the boundaries. This seems to show that the vertical field boundaries have a strong influence on the turbulence. I will come back to this transition later.

2.2.3 Pm dependence

In order to check whether the convergence problem is present in this set up, I did a few runs with different values of the magnetic Prandtl number for Rm = 100. No strong variation of the turbulence intensity with Pm is visible (Figure 2.8), the left-most and right-most points with lower magnetic field values and larger error bars may be explained by the fact that the magnetic field was still slowly growing and had probably not yet reached its final level in those runs (while the rms value of the velocity field was steady). The absence of a convergence problem may be due to the presence of stratification (stratified MRI simulations are known to have no convergence problem) or to the use of vertical field boundary conditions (which in the zero net flux case also remove the convergence problem).

I did not carry this study further as I wanted to first understand better the effects of the vertical field boundary conditions, which is done in Section 2.3.

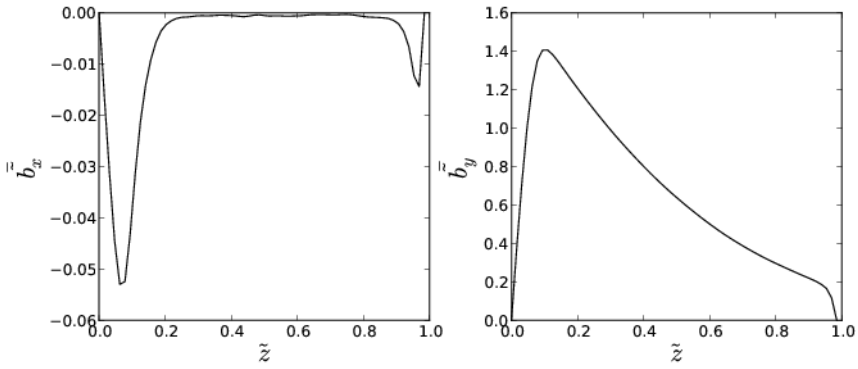

Figure 2.7: Profiles of the mean magnetic field after the transition (averaged over 70 orbital times).

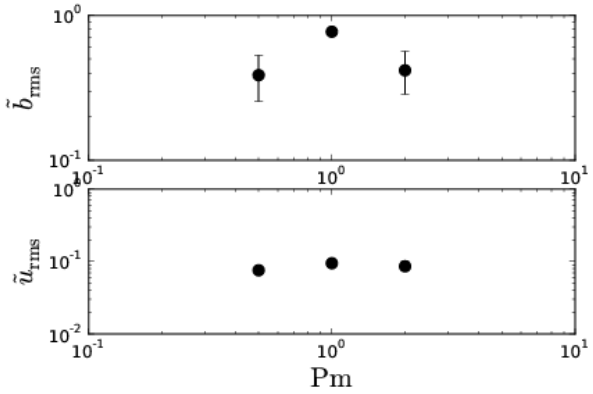

Figure 2.8: Pm dependence of the turbulence intensity in the final state measured by the time averaged rms values of the variables.

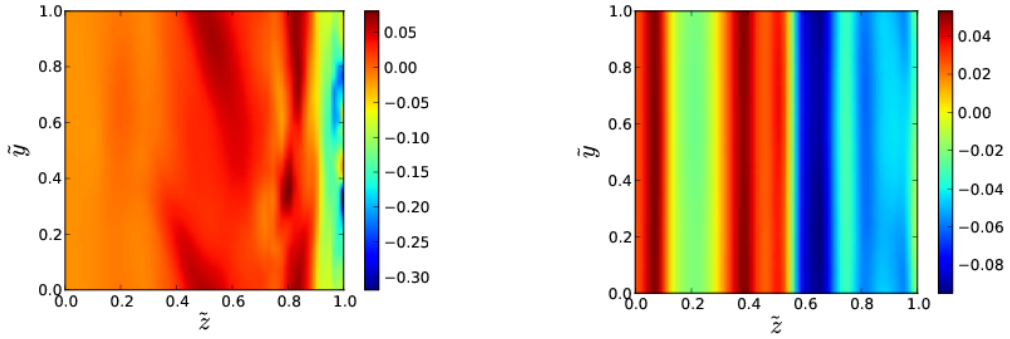

Figure 2.9: Snapshots of the x component of the velocity field in a yz-plane, before the transition (left, $\tilde{t} = 30$) and in the final state (right, $\tilde{t} = 180$).

2.2.4 Y-invariance

Another surprising result concerning the transition (cf. Section 2.2.2) is that the variables appear to become almost completely y-independent in the final stage, while it was reasonably y-dependent just after the saturation. Figure 2.9 illustrates this point.

In order to see more precisely this transition, we can construct an indicator of y-variability by comparing the full magnetic energy to the magnetic energy calculated from the y-averaged field:

$$\mathrm{M} = \int\int\int dx\ dy\ dz\ b^2, \quad \mathrm{M}_y = \int\int dx\ dy\ dz\ \bar{b}^2 \quad \text{and} \quad I_y = \frac{\mathrm{M} - \mathrm{M}_y}{\mathrm{M}}$$

where $\bar{b} = \int dy\ b/L_y$ is the y-averaged magnetic field. It measures the fraction of the magnetic energy present in the fluctuations along y (the same thing could be done with kinetic energy).

The evolution of this indicator (Figure 2.10) shows at first a plateau just after the saturation, followed by a sudden decrease when the rms magnetic field starts to grow again. It then stays at very low values.

This transition seems to be related with the transition in the mean field profile, but I did not find an explanation for any of those two phenomena.

2.2.5 Mean field tensors α and η

In a mean field theory perspective, I tried to measure the α and η tensors in the final state by using the testfield method described earlier, using the simplest (non k-dependent) testfields. The resulting profiles are averaged over several tens of orbital times in the final state and are shown on Figure 7.

The first meaningful result is that α_{yy} and η_{yx} are very small compared to the other components. This is an effect of the 2D behavior of the final state as one find that in a 2D situation the testfield method can give only zero for those two coefficients. It can be understood as a consequence of Cowling's anti-dynamo theorem, saying that no dynamo

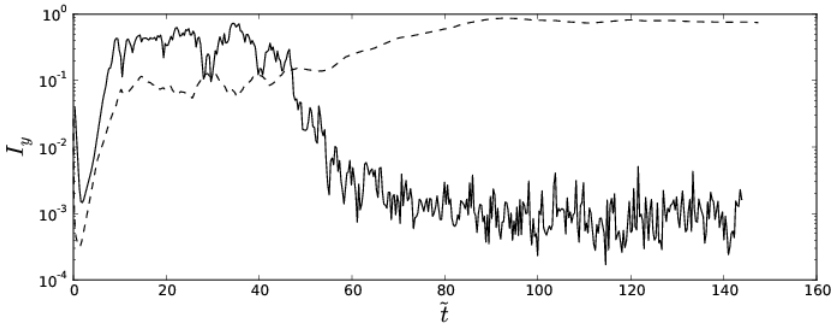

Figure 2.10: Time evolution of the indicator of y-variability I_y. The superimposed dashed line recalls the time evolution of $\tilde{b}_{\mathrm{rms}}$

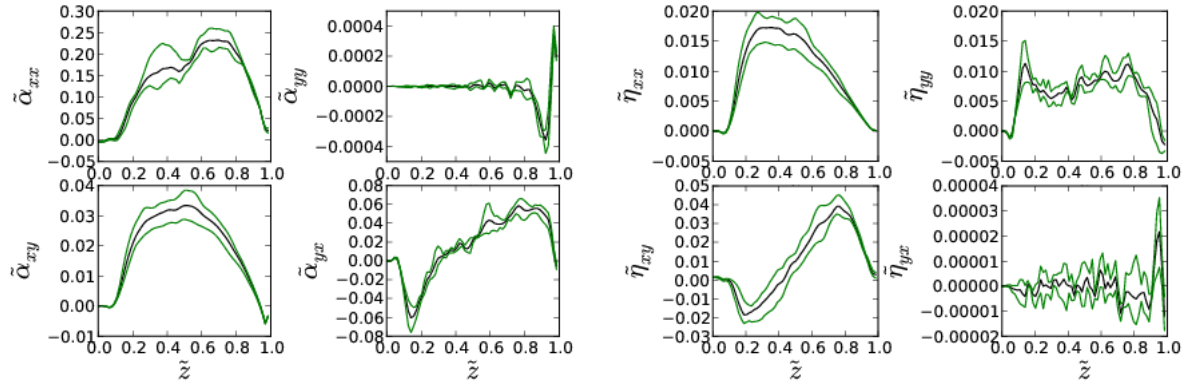

Figure 2.11: Profiles of the coefficients of the dimensionless tensors $\tilde{\alpha} = \frac{\alpha}{c_s}$ and $\tilde{\eta} = \frac{\eta}{c_s L}$. Green lines show the error bars.

is possible for axisymmetric fields (which is equivalent to y-independence in our local approximation), as those two components are the only ones which could create b_x field from the b_y field and thus close the dynamo cycle (the presence of shear create b_y field from the b_x field).

One can also note the difference between the profiles η_{xx} and η_{yy} (turbulent diffusivity behave differently in the x and y directions) which may be a consequence of the anisotropy due to the presence of the shear flow. When trying to reconstruct the electromotive force, we get a result that is one order of magnitude too big, indicating that the testfield method as it was used here was inadequate. I did not investigate this further as I then focused on the situation described in the next section, but this problem occurred again and will be discussed later.

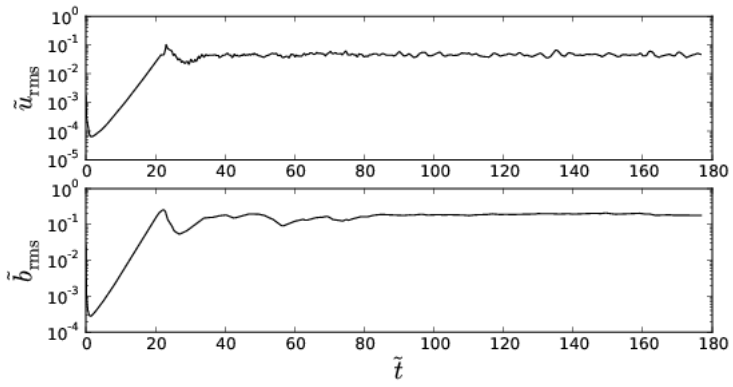

Figure 2.12: Time evolution of the root mean square values of the velocity and magnetic fields in an unstratified simulation

2.3 Unstratified simulations with vertical field boundary conditions

2.3.1 Introduction

In order to understand the effect of vertical field boundary conditions that seemed to play a very strong role in my stratified simulations, I tried to study this effect independently of the effect of stratification. I used simulations with exactly the same setup as in the last section, except for the gravity field that was removed.

The goal was to see if the transition observed before was an effect of stratification or not, but also to see if the strong gradients and peaks near the boundaries are still present. In a mean field theory perspective, I was still interested in measuring the α and η tensors to parametrize a mean field model. Moreover, as this setup is exactly the same (except for the uniform imposed field) as the one used in Käpylä & Korpi (2010) [6], in which it is shown that the convergence problem disappears when using vertical field boundary conditions in the zero net flux case, I wanted to confirm this result in the finite net flux case.

2.3.2 Time series and mean field structure

As in the previous sections, the time evolution (Figure 2.12) of the rms magnetic and velocity fields shows at first an exponential growth with a growth rate consistent with the analytical prediction, followed by the saturation into a statistically steady turbulent state. This time no transition appears in the time series. However, once again, when looking at the evolution of the mean magnetic field (Figure 2.13), a transition is visible. This time, we see a very clear change of the geometry of the mean field: from an antisymmetric profile, positive in one half of the box and negative in the other one, it switches to a symmetric, almost uniform profile. The change is quite quick and occurs a few tens of

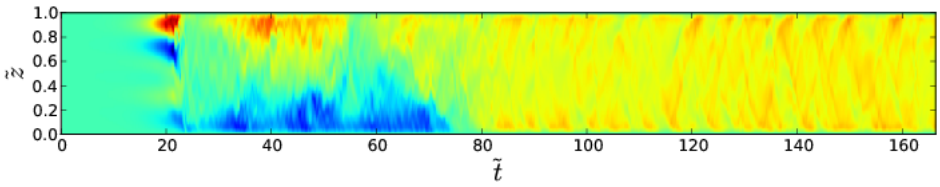

Figure 2.13: Time evolution of the y component of the mean magnetic field

orbital times after the end of the exponential growth, as in the stratified simulations.

The time averaged profiles are shown in Figure 2.14, comparing the two stages. Once again, strong gradients and peaks are present near the boundaries, confirming the presence of a strong current sheet near the boundaries. This horizontal current sheet and the vertical external field should create a horizontal flow at the same place. This mean flow is indeed observed, its x component being exactly the one calculated from the equilibrium between the Lorentz force due to the measured mean magnetic field, the Coriolis force and the effect of the imposed shear flow only. The y component has the right sign and shape, but is too big by a factor of 4, showing an influence from the turbulent Lorentz force.

As the strong magnetic gradient near the boundary was occurring on a length corresponding to a few grid points only, I checked if it could be a numerical artifact by doubling the resolution. However, higher resolution (128^3) runs show the same length scale as the corresponding usual resolution (64^3) runs. This length scale varies roughly linearly with Re and Rm.

This confirms the very strong effect of vertical field boundary conditions: the strong diffusion that occurs in the current sheet must be compensated in the final steady state. The electromotive force from the mean flow and mean magnetic field is negligible compared to the dissipation. So it is the turbulent EMF that sustains the field. It seems then that the most important part of the effect of the turbulence is occurring in the neighborhood of the boundaries. Vertical field boundary conditions could thus be a bad choice when trying to study MRI-driven turbulence.

2.3.3 Pm dependence

Exploring the variations with Pm of turbulence intensity and the α_{SS} parameter confirmed that there is no convergence problem when using vertical field boundary conditions, even in the finite net flux case. Pm was varied between 0.5 and 2. However, limitations due to resolution prevented me to keep Rm constant at the same time. Rm

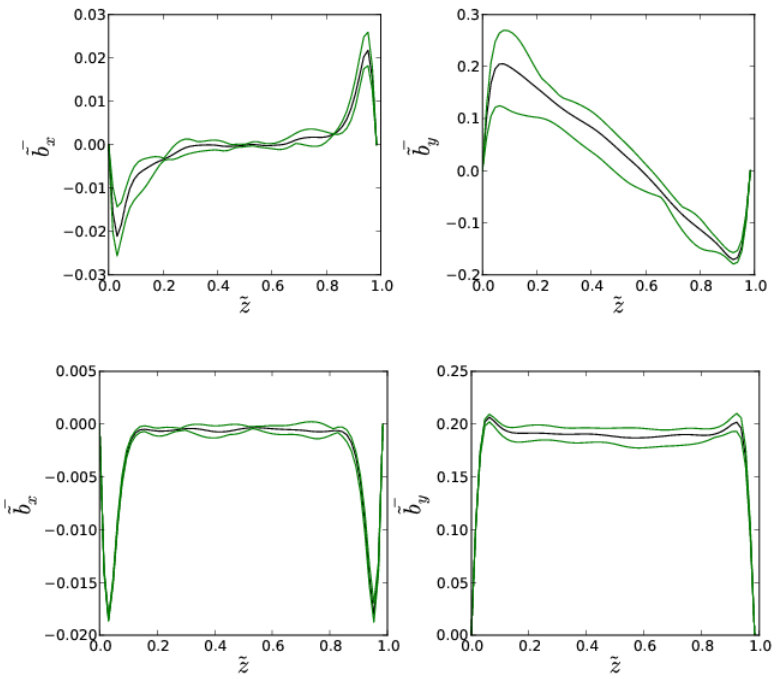

Figure 2.14: Profiles of the x (left) and y (right) components of the mean magnetic field before (top) and after the transition (bottom). Green lines show the error bars.

varied between 50 and 100. The parameters of the runs and their results are summarized in Table 2.1.

Run	Pm	Rm	$\tilde{u}_{rms}$	$\tilde{b}_{rms}$	$\alpha_{\rm SS}$	$\lvert\overline{\tilde{b}_y}\rvert$
A	1.	100	0.05014	0.2029	0.04965	0.1939
B	0.5	50	0.04161	0.2417	0.03605	0.2201
C	2.	100	0.04586	0.1865	0.02641	0.1815
D	1.5	100	0.05006	0.1974	0.03531	0.1971
E	0.66	66	0.04516	0.2072	0.03344	0.1994

Table 2.1: Set of unstratified runs exploring the dependence in Pm

Once again, no systematic variation with Pm is found. One can also see in the table that the root mean square magnetic field is actually dominated by the y component of the mean magnetic field.

2.3.4 Y-invariance

Another result that is reminiscent of the stratified runs of the previous section is that the fields become almost two-dimensional after the transition, while variations along y were

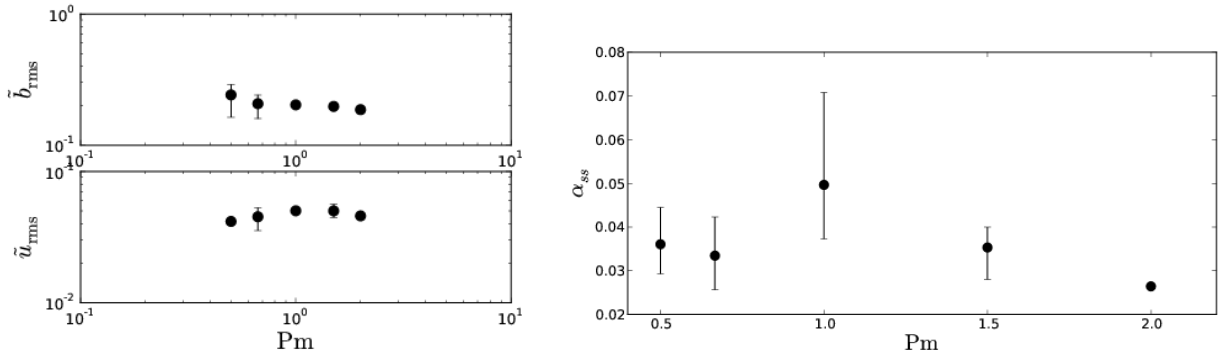

Figure 2.15: Influence of Pm on the rms values of the turbulence (left), and on the $\alpha_{\rm SS}$ parameter (right) for unstratified simulations.

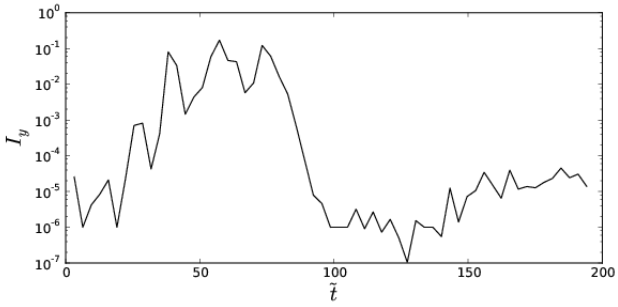

Figure 2.16: Time evolution of the indicator of y-variability I_y

present just after saturation. We can once again use our indicator. However, this time, as the full data were not saved for disk space limitation reasons, it will only be calculated on a xy-plane, giving less accurate and more fluctuating results, with a different order of magnitude.

But it is still possible to see that the y-variations vanish roughly at the time at which the geometry of the mean field switches from antisymmetric to symmetric. Figure 2.16 shows this evolution.

As a confirmation that the final state is really two-dimensional, 2D runs with the same setup lead to this same final state. More interestingly, the evolution toward this state seems to be also the same: after the saturation, a transitory stage with an antisymmetric mean field is followed by a sudden transition leading to the final state, as shown in Figure 2.17.

As in the stratified case, I did not find an explanation of this transition. The surprising fact is that the transitory state just after the transition follows the same evolution regardless of whether it is in a 3D state (3D simulation) or in a 2D state (2D simulation).

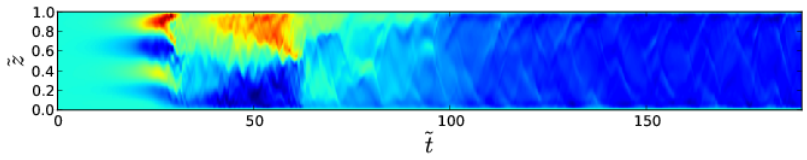

Figure 2.17: Time evolution of the y component of the mean magnetic field in a 2D simulation.

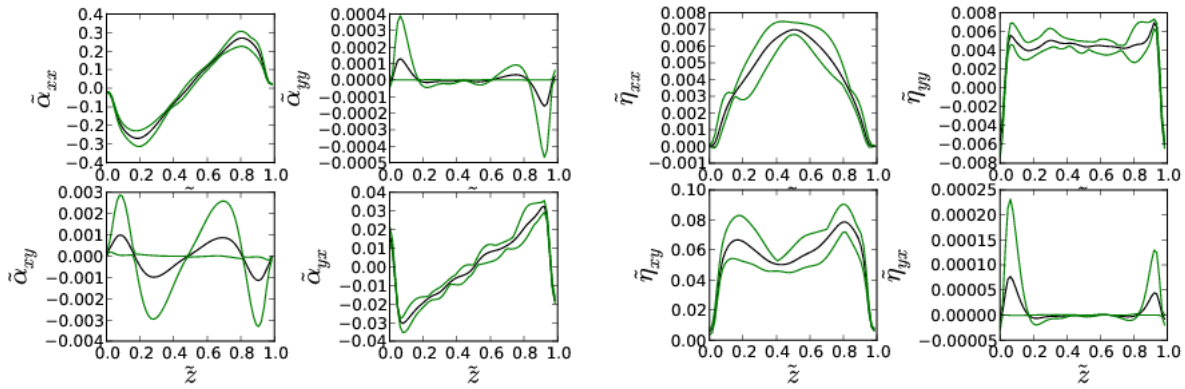

Figure 2.18: Profiles of the coefficients of the dimensionless tensors $\tilde{\alpha} = \frac{\alpha}{c_s}$ and $\tilde{\eta} = \frac{\eta}{c_s L}$. Green lines show the error bars.

2.3.5 Mean field coefficients and reconstruction of the EMF

The measurement of the α and η tensors, using the testfield method with simple linear testfields gives very similar results to those that were obtained in stratified runs (Figure 2.18). The α_{yy} and η_{yx} components are negligible compared to the others, as a consequence of the approximate y-invariance. The anisotropy of the flow is clearly visible in the difference between η_{xx} and η_{yy}. It also appears that doing those measurements in equivalent 2D runs gives very similar results, confirming again the approximate two-dimensionality of the turbulence.

But the EMF reconstructed from these measured tensors does not correspond to its measured value, it is more than one order of magnitude too large. Two possible reasons may explain this problem. As a uniform B_z field is present, α_{xz} and α_{yz} should be taken into account, as they may have an effect through the z-derivative of these coefficients. I added one more testfield to measure these coefficients, but it appeared that they do not

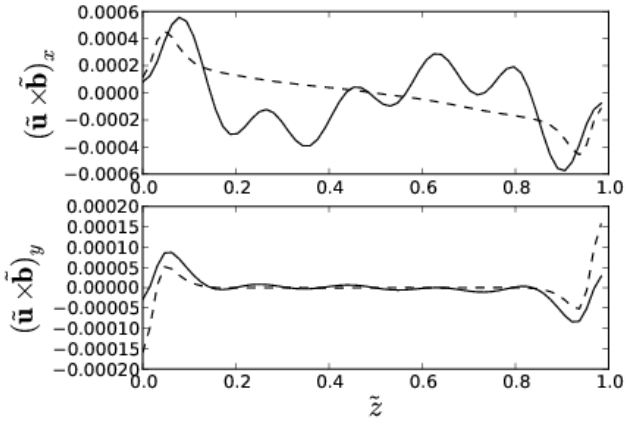

Figure 2.19: Reconstruction of the EMF from the Fourier space α and η tensors, averaged over time in the final saturated state (solid line), and comparison with the measured profile (dashed line).

solve the problem.

The other explanation may be that the simple ansatz taking into account only the first derivative is not sufficient in this case, and that effects from higher derivatives are not negligible. In order to test this hypothesis, I measured the tensor coefficients for different sets of sinusoidal testfields with dimensionless wavenumbers from 0 to 5. The reconstruction of the EMF via the more complex ansatz (1.22) gives a better result (Figure 2.19). It has the right order of magnitude, and the y component fits relatively well the measured profile. It seems however that higher wave numbers would be necessary to have a good reconstruction of both components.

The next step in order to get a predictive mean field model would be to find out the relation between these k-dependent tensors and the mean magnetic field and mean flow, which is a much more complex problem.

2.4 Other boundary conditions

The previous results concerning the use of vertical field boundary conditions are rather unsatisfactory: it seems that the boundaries are the dominant effect, which is not the one we would like to study. Therefore I tried to use other kinds of boundary conditions.

2.4.1 High diffusivity halos

A good way to reduce the effect of the boundaries is to introduce two zones between the main part of the domain and the top and bottom boundaries in which the magnetic diffusivity η is very high. The magnetic field is damped before reaching the boundaries, and thus the constraint at the boundary has a weaker effect.

I tried this solution with various configurations: size of each halo varying between 50% and 100% of the size of the main domain, diffusivity in the halo part between 10 and 100 times larger than the diffusivity in the main domain, various widths for the transition of η at the interfaces between the halos and the main domain.

It appeared that a numerical instability is present in this situation, which I did not manage to avoid. It first appeared by making the runs crash. In some 2D cases, it was not crashing, and I could see the evolution. The mean field structure in the final stage is relatively reminiscent of the case without halos, but with much smoother variations at the interface with the halos.

However, not all results in this case are reliable as the numerical instability is still present, clearly apparent in the testfield calculations, and is probably also affecting the main run.

2.4.2 Vacuum boundary conditions

Another less constraining boundary condition for the top and bottom boundaries is the vacuum boundary condition. In order to have a decaying field in the ghost zones which follows $\Delta \boldsymbol{A} = 0$, the Fourier transform of the field on the plane of the boundary is calculated, and each mode decays in the ghost zones with the right decay rate.

It seems that the implementation of this boundary condition was not working properly, and I did not manage to find a way to make it work.

Conclusion

After familiarizing myself with the magneto-rotational instability and with the use of the Pencil Code, I started studying a certain number of subjects. The study of the effect of a constant gravity field made apparent the strong effect of vertical field boundary conditions, and led me to investigate this effect independently. At the same time, I confirmed that the convergence problem was not present in these situations, and showed that simple linear testfields are not sufficient to capture the relationship between the fluctuating electromotive force and the mean magnetic field, but that a k-dependent formalism may be adequate if high enough values of k are taken into account.

Moreover, this internship was for me the occasion to learn how to search in the scientific literature and to use the help of tools like ADS or the ArXiv. It was an occasion via a lot of reading to learn about a wide field of physics deriving from magnetohydrodynamics: the study of turbulence and mean field theories, in particular mean field dynamo theory and its fields of application in astrophysics. I also discovered the functioning of a research group (which I would like to thank again for their welcome and help), the world of numerical computing and supercomputers, and a beautiful country.

Bibliography

[1] Balbus, S. A., Hawley, J. F. 1998, *Reviews of Modern Physics*, 70, 1

[2] Shakura, N. I., Sunyaev, R. A. 1973, *Astronomy & Astrophysics*, 24, 337

[3] Balbus, S. A., Hawley, J. F. 1991, *The Astrophysical Journal*, 376, 214

[4] Fromang, Papaloizou, Lesur, Heinemann 2007, *Astronomy & Astrophysics*, 476, 1123

[5] Lesur, G.; Longaretti, P.-Y. 2007, *Monthly Notices of the Royal Astronomical Society*, 378, 1471-1480

[6] Käpylä, P. J., Korpi, M. J. 2010, *Monthly Notices of the Royal Astronomical Society* (submitted)

[7] Moffatt, H. K. 1978, Magnetic field generation in electrically conducting fluids. (Cambridge University Press)

[8] Krause F, Rädler K-H. 1980. Mean-Field Electrodynamics and Dynamo Theory. Berlin: Akademie-Verlag; Oxford: Pergamon

[9] Schrinner, M.; Rädler, K.-H.; Schmitt, D.; Rheinhardt, M.; Christensen, U. 2005, *Astronomische Nachrichten*, 326, 3, 245-259

[10] Schrinner, M.; Rädler, K.-H., Schmitt, D., Rheinhardt, M., Christensen, U. R. 2007, *Geophysical & Astrophysical Fluid Dynamics*, 101, 2, 81-116

[11] Rheinhardt, M.; Brandenburg, A. 2010, *Astronomy & Astrophysics* (in press), DOI: 10.1051/0004-6361/201014700